Tunable magnon blockade in a magnon-qubit system with coherent and parametric driving

Yuchen Liu,[1] Binhui Chang,[1] Cong Cui,[3] Xinping Li,[2] Hongzhi Shen,[3,*]
Xiaofeng Duan,[1,†] Junhua Hou,[1,2,‡], Tianze Luan,[4] and Wenyao Hu,[3]
[1]*College of Physics and Electronic Engineering, Shanxi Normal University, Taiyuan 030031, China*
[2]*Shanxi Provincial Education Examination and Question Paper Center, Taiyuan 030000, China*
[3]*Center for Quantum Sciences and School of Physics, Northeast Normal University, Changchun 130024 China*
[4]*School of Physics Science and Technology, Shenyang Normal University, Shenyang 110034, China*

(Dated: September 29, 2026)

We study the magnon antibunching effect in the magnon-qubit coupling system under the joint action of coherent and parametric drives. The analysis and numerical results reveal the conventional magnon blockade (CMB) caused by the anharmonic level splitting induced by strong magnon–qubit coupling and the unconventional magnon blockade (UMB) induced by multipath destructive interference. Notably, in the strong-coupling regime, substituting the CMB condition into the optimal UMB condition yields a phase-tuned CMB-constrained UMB condition, which simultaneously realizes strong magnon antibunching and a high single-magnon occupation probability. This combines the high brightness afforded by CMB with the high purity provided by UMB. Furthermore, in the weak-coupling regime, coordinated tuning of the phase, detuning, parametric drive, and coupling strength induces destructive interference among distinct excitation pathways, thereby yielding the UMB effect. Importantly, even in the zero-coupling limit, the additional channel provided by the parametric drive can sustain this blockade. This flexibility removes the reliance on stringent strong-coupling constraints, offering a viable route toward tunable strong magnon antibunching.

PACS numbers: 42.50.-p, 42.50.Pq, 75.30.Ds, 85.25.Dq
Keywords: conventional magnon blockade, unconventional magnon blockade, magnon antibunching, destructive interference

I. INTRODUCTION

Magnons are quantized quasiparticles of spin-wave excitations in magnetic materials, originating from collective excitations of the spin system [1–3]. To date, high-spin-density ferromagnetic systems have been investigated on a variety of platforms, including ultracold atomic ensembles [4], nitrogen-vacancy (NV) centers in diamond [5–7], and molecular nanomagnets coupled to cavities [8]. Among these, ferrimagnetic yttrium iron garnet (YIG) holds a prominent position in hybrid magnonic systems, owing to its high spin density ($\rho_s = 4.22 \times 10^{27}\mathrm{m}^{-3}$), low damping rate ($\alpha_G \sim 10^{-5} - 10^{-4}$), and nonlinear tunability arising from spin-wave excitations [9]. In the YIG-superconducting qubit system, both direct exchange coupling [9] and microwave-cavity-mediated indirect coupling [10–15] have been demonstrated theoretically [10, 11] and experimentally [12–16], rendering this hybrid architecture a key platform for quantum information processing.

In mesoscopic hybrid magnonic systems based on YIG spheres, a rich variety of physical phenomena have been observed. According to the underlying physical mechanisms, they fall into two categories: macroscopic classical effects driven by strong nonlinearity, including bistability [17, 18], multistability [19], magnon frequency combs [20, 21], and mesoscopic quantum effects reflecting quantum coherence, such as magnon superradiance [22], ground-state sideband cooling [23], and the preparation of squeezed magnon states [24, 25]. Spurred by these advances, significant progress has been made in quantum manipulations at the microscopic scale. In quantum state engineering, these achievements encompass the preparation of magnon Fock states and their superpositions [26–29], magnon-magnon entanglement within microwave cavities [30, 31] and cavity arrays [32], magnon-photon-phonon tripartite entanglement [33, 34], and magnon-photon Bell states [35, 36]. In coherent dynamics, microwave sideband cooling [37] and coherent information storage in magnon dark modes [38] have been successfully implemented. In functional applications, these single-excitation-level manipulations lay an important foundation for quantum transducers [39–41] and highly sensitive quantum sensors [42–45].

The magnon blockade (MB) effect has attracted considerable interest in quantum statistical studies. Analogous to photon blockade, its underlying mechanism stems from nonlinear effects [46–57] or quantum interference [58–73]. Specifically, the antibunching arising from energy-level anharmonicity is termed conventional magnon blockade (CMB) [74], whereas that stemming from multipath quantum interference is referred to as unconventional magnon blockade (UMB) [75–78]. Compared with the qubit-magnon system without parametric driving [79], our scheme introduces a parametric drive that provides an additional interference channel and a tunable

*Corresponding author: shenhz458@nenu.edu.cn
†Corresponding author: dxfhjh2002@163.com
‡Corresponding author: jhhou@sxnu.edu.cn

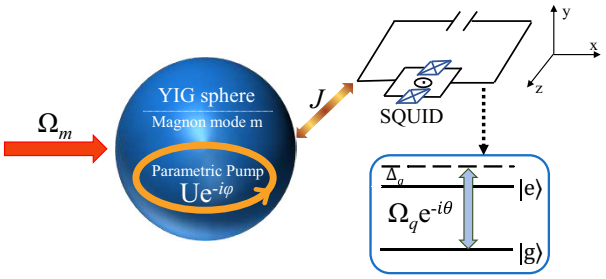


FIG. 1: Schematic of a hybrid magnon-qubit system. The YIG sphere interacts with the superconducting transmon qubit through the coupling strength J, and a parametric drive $Ue^{-i\varphi}$ is applied to the YIG sphere, providing an additional two-magnon excitation pathway. The YIG sphere and the superconducting transmon qubit are driven by two microwave fields with Rabi frequencies Ω_m and Ω_q, respectively, and with a relative phase difference θ.

phase. In contrast to the nonreciprocal MB based on the interference between coherent and dissipative couplings [80], we focus on the cooperative effect of coherent driving and parametric driving. Different from the waveguide system with a giant spin ensemble and a giant atom [81], where the magnon and qubit are coupled indirectly through a common waveguide, our system employs a direct exchange coupling between the YIG sphere and the transmon qubit via a SQUID loop.

This work constructs a hybrid magnon-qubit system by directly coupling a YIG sphere with a superconducting transmon qubit and introducing a parametric drive for the magnon mode, and studies the UMB and CMB effects in this system. This system leverages the high sensitivity of the superconducting quantum interference device (SQUID) to external magnetic flux to regulate the transverse coupling between magnon and qubit. To enhance the MB effect, we drive both the qubit and the magnon, and introduce adjustable phases θ and φ into the qubit drive and parametric drive, respectively. In the strong-coupling regime, we derive the CMB-constrained optimal UMB condition, which simultaneously achieves strong magnon antibunching and high single-magnon occupation probability. In the weak-coupling regime, we derive the optimal UMB conditions and find that the blockade depends on the coordinated action of the detuning, coupling strength, and both the amplitude and phase of the parametric drive.

II. MODEL

In this paper, we consider a hybrid magnon-qubit system [16], as shown in Fig. 1. In this system, the magnons generated in the YIG sphere are magnetically coupled to the SQUID loop of the superconducting transmon qubit through the flux variation $\Phi(\Delta u)$, which is caused by the magnetic moment fluctuation Δu of the magnons. This interaction leads to a transverse exchange coupling between the magnon and the qubit with coupling strength J [12, 82]. Additionally, we apply a parametric drive $Ue^{-i\varphi}$ (amplitude U and phase φ) to the YIG sphere to provide an additional two-magnon excitation pathway. On this basis, by driving the magnon and the qubit, respectively, the MB effect is realized [83–85]. The total Hamiltonian reads ($\hbar \equiv 1$)

$$\begin{aligned}\hat{H}_{\rm tot} &= \omega_q \hat{\sigma}_+\hat{\sigma}_- + \omega_m \hat{m}^\dagger \hat{m} + J(\hat{m}\hat{\sigma}_+ + \hat{m}^\dagger\hat{\sigma}_-) \\ &+ \Omega_m(\hat{m}^\dagger e^{-i\omega t} + \hat{m}e^{i\omega t}) \\ &+ \Omega_q[\hat{\sigma}_+ e^{-i(\omega t+\theta)} + \hat{\sigma}_- e^{i(\omega t+\theta)}] \\ &+ U[\hat{m}^2 e^{i(\omega_p t+\varphi)} + \hat{m}^{\dagger 2} e^{-i(\omega_p t+\varphi)}],\end{aligned} \tag{1}$$

where the first and second terms on the right side of the equation describe the free Hamiltonian of the qubit with eigenfrequency ω_q and the magnon with eigenfrequency ω_m, respectively. The third term represents the magnon-qubit exchange coupling with strength J. The fourth and fifth terms drive, respectively, the magnon mode (with intensity Ω_m) and the qubit (with intensity Ω_q and phase θ). The last term represents the parametric drive of the magnon mode, with amplitude U and phase φ. We assume that the magnon drive and the qubit drive share the same frequency ω, while the two-magnon parametric drive has frequency $\omega_p = 2\omega$. By using the rotation operator $\hat{R}(t) = \exp[-i\omega t(\hat{m}^\dagger\hat{m} + \hat{\sigma}_+\hat{\sigma}_-)]$, we can eliminate the time dependence of $\hat{H}_{\rm tot}$, and the effective Hamiltonian can be described as

$$\begin{aligned}\hat{H}_{\rm eff} &= \Delta_q \hat{\sigma}_+\hat{\sigma}_- + \Delta_m \hat{m}^\dagger\hat{m} + J(\hat{m}\hat{\sigma}_+ + \hat{m}^\dagger\hat{\sigma}_-) \\ &+ \Omega_m(\hat{m}^\dagger + \hat{m}) + \Omega_q(\hat{\sigma}_+ e^{-i\theta} + \hat{\sigma}_- e^{i\theta}) \\ &+ U(\hat{m}^2 e^{i\varphi} + \hat{m}^{\dagger 2} e^{-i\varphi}),\end{aligned} \tag{2}$$

where $\Delta_q = \omega_q - \omega$ and $\Delta_m = \omega_m - \omega$ represent the detunings of the qubit and the magnon from the microwave drive frequency, respectively. We take the phase of the magnon drive as the reference. Then θ is the phase of the qubit drive relative to the magnon drive, and φ is the phase of the parametric drive relative to 2ω. The physically observable phases are θ and φ. We adopt the non-resonant condition $\Delta_q \neq \Delta_m$ for the strong-coupling CMB and UMB [86–88], and the resonant condition $\Delta_q = \Delta_m = \Delta$ for the weak-coupling UMB [89, 90].

Dissipation is an inherent property of open quantum systems. It serves as both an inevitable source of attenuation in experiments and a dynamical element that must be incorporated into theoretical models. In the hybrid magnon-qubit open system that we have studied, dissipation is primarily manifested through the Gilbert damping rate κ_m of the magnon and the relaxation rate κ_q of the qubit. The dissipative dynamics can be described by introducing Lindblad operators into the quantum master equation [91], allowing further calculation of the magnon statistics in the steady state. The master equation reads

$$\begin{aligned}\frac{\partial\hat{\rho}}{\partial t} &= -i[\hat{H}_{\rm eff},\hat{\rho}] + \frac{\kappa_m}{2}(2\hat{m}\hat{\rho}\hat{m}^\dagger - \hat{m}^\dagger\hat{m}\hat{\rho} - \hat{\rho}\hat{m}^\dagger\hat{m}) \\ &+ \frac{\kappa_q}{2}(2\hat{\sigma}_-\hat{\rho}\hat{\sigma}_+ - \hat{\sigma}_+\hat{\sigma}_-\hat{\rho} - \hat{\rho}\hat{\sigma}_+\hat{\sigma}_-).\end{aligned} \tag{3}$$

For simplicity, in the following discussion we set $\kappa_m = \kappa_q = \kappa$ and fix the relative phase of the qubit drive at $\theta = 0$,

unless otherwise specified. The phase φ of the parametric drive is the main tuning parameter for the UMB effect. The quantum statistical properties of the magnon can be characterized using the equal-time second-order correlation function [92]

$$g^{(2)}(0)=\frac{\mathrm{Tr}(\hat{\rho}\hat{m}^{\dagger}\hat{m}^{\dagger}\hat{m}\hat{m})}{[\mathrm{Tr}(\hat{\rho}\,\hat{m}^{\dagger}\hat{m})]^{2}}=\frac{\langle\hat{m}^{\dagger}\hat{m}^{\dagger}\hat{m}\hat{m}\rangle}{\langle\hat{m}^{\dagger}\hat{m}\rangle^{2}}, \tag{4}$$

where the steady-state density matrix $\hat{\rho}$ can be obtained from the master equation given in Eq. (3). Numerical simulations are performed using the Quantum Optics Toolbox in MATLAB. The master equation is solved with the magnon mode truncated at $N=6$, with the qubit treated as a two-level system. The steady-state solver uses a convergence tolerance of 10^{-12}. The cases $g^{(2)}(0)<1$ and $g^{(2)}(0)>1$ correspond to the antibunching and bunching effects of magnons, respectively; that is, the magnon number follows sub-Poissonian or super-Poissonian statistics. In particular, $g^{(2)}(0)\to 0$ indicates that the magnons in the YIG sphere are blockaded, i.e., two- and higher-magnon occupation is strongly suppressed.

III. ANALYTICAL OPTIMAL CONDITIONS AND SECOND-ORDER CORRELATION FUNCTIONS

To determine the optimal conditions for CMB, the undriven Hamiltonian is expanded in the single-excitation basis states $|g,1\rangle$ and $|e,0\rangle$, yielding the matrix

$$\hat{H}_0=\begin{pmatrix}\omega_m & J\\ J & \omega_q\end{pmatrix}. \tag{5}$$

Diagonalizing the matrix yields

$$E_1^{1,2}=\frac{\omega_m+\omega_q}{2}\mp\sqrt{\frac{(\omega_m-\omega_q)^2}{4}+J^2}. \tag{6}$$

When the driving frequency is tuned to $\omega=E_1^{1,2}$, single-magnon resonant absorption enhances the population of the single-magnon state. Hence, the optimal condition for CMB is

$$\Delta_m\Delta_q=J^2. \tag{7}$$

Next, we discuss the UMB case. Under weak driving, the Hilbert space is truncated to the zero-, one-, and two-magnon states, and the wave function of the system can be expressed as

$$\begin{aligned}|\psi\rangle=&C_{g,0}|g,0\rangle+C_{g,1}|g,1\rangle+C_{e,0}|e,0\rangle\\&+C_{e,1}|e,1\rangle+C_{g,2}|g,2\rangle.\end{aligned} \tag{8}$$

Here, $C_{g(e),n}$ and $|C_{g(e),n}|^2$ are the probability amplitude and probability, respectively, of finding the system in the state $|g(e),n\rangle=|g(e)\rangle\otimes|n\rangle$, where the qubit is in the ground or excited state and the magnon mode contains n excitations.

Under the weak driving condition, we have $|C_{g,0}|\approx 1\gg|C_{e,0}|,|C_{g,1}|\gg|C_{e,1}|,|C_{g,2}|$. Combining Eqs. (4) and (8), we obtain the second-order correlation function $g^{(2)}(0)\approx 2|C_{g,2}|^2/|C_{g,1}|^4$. The coefficients $C_{g(e),n}$ are obtained by solving the Schrödinger equation, which then gives $g^{(2)}(0)$. Substituting $\hat{H}=\hat{H}_{\mathrm{eff}}-i(\kappa_q\hat{\sigma}_+\hat{\sigma}_-+\kappa_m\hat{m}^{\dagger}\hat{m})/2$ [$\hat{H}_{\mathrm{eff}}$ is given by Eq. (2)] and Eq. (8) into $i\partial_t|\psi\rangle=\hat{H}|\psi\rangle$, we obtain [93, 94]

$$\begin{aligned}
i\dot{C}_{g,1}&=(\Delta_m-\frac{i\kappa_m}{2})C_{g,1}+JC_{e,0}+\Omega_mC_{g,0},\\
i\dot{C}_{e,0}&=(\Delta_q-\frac{i\kappa_q}{2})C_{e,0}+JC_{g,1}+\Omega_qe^{-i\theta}C_{g,0},\\
i\dot{C}_{e,1}&=(\Delta_q-\frac{i\kappa_q}{2})C_{e,1}+(\Delta_m-\frac{i\kappa_m}{2})C_{e,1}+\sqrt{2}JC_{g,2}\\
&\quad+\Omega_mC_{e,0}+\Omega_qe^{-i\theta}C_{g,1},\\
i\dot{C}_{g,2}&=\sqrt{2}(JC_{e,1}+\Omega_mC_{g,1}+Ue^{-i\varphi}C_{g,0})\\
&\quad+2(\Delta_m-\frac{i\kappa_m}{2})C_{g,2}.
\end{aligned} \tag{9}$$

In the steady state, Eq. (9) reduces to

$$\begin{aligned}
0&=(\Delta_m-\frac{i\kappa_m}{2})C_{g,1}+JC_{e,0}+\Omega_m,\\
0&=(\Delta_q-\frac{i\kappa_q}{2})C_{e,0}+JC_{g,1}+\Omega_qe^{-i\theta},\\
0&=(\Delta_q-\frac{i\kappa_q}{2})C_{e,1}+(\Delta_m-\frac{i\kappa_m}{2})C_{e,1}+\sqrt{2}JC_{g,2}\\
&\quad+\Omega_mC_{e,0}+\Omega_qe^{-i\theta}C_{g,1},\\
0&=\sqrt{2}(JC_{e,1}+\Omega_mC_{g,1}+Ue^{-i\varphi})+(2\Delta_m-i\kappa_m)C_{g,2}.
\end{aligned} \tag{10}$$

From Eq. (10), we obtain

$$C_{g,1}=\frac{\overline{\Delta}_q\Omega_m-J\Omega_qe^{-i\theta}}{J^2-\overline{\Delta}_q\overline{\Delta}_m}, \tag{11}$$

$$\begin{aligned}C_{g,2}=&\frac{(\overline{\Delta}_m+\overline{\Delta}_q)\Theta Ue^{-i\varphi}-[\overline{\Delta}_q(\overline{\Delta}_m+\overline{\Delta}_q)+J^2]\Omega_m^2}{\sqrt{2}\Theta(\overline{\Delta}_m^2+\overline{\Delta}_m\overline{\Delta}_q-J^2)}\\&+\frac{2(\overline{\Delta}_m+\overline{\Delta}_q)e^{-i\theta}J\Omega_m\Omega_q-e^{-2i\theta}J^2\Omega_q^2}{\sqrt{2}\Theta(\overline{\Delta}_m^2+\overline{\Delta}_m\overline{\Delta}_q-J^2)},\end{aligned} \tag{12}$$

where $\overline{\Delta}_m=\Delta_m-i\kappa_m/2$, $\overline{\Delta}_q=\Delta_q-i\kappa_q/2$, and $\Theta=\overline{\Delta}_m\overline{\Delta}_q-J^2$. UMB suppresses the two-magnon probability through destructive interference, while the single-magnon occupation probability is unaffected. Since $g^{(2)}(0)=2|C_{g,2}|^2/|C_{g,1}|^4$ in the weak-driving regime, the optimal UMB condition $g^{(2)}(0)=0$ is equivalent to $C_{g,2}=0$. Setting the numerator of Eq. (12) to zero gives

$$\begin{aligned}&\Big|(\overline{\Delta}_m+\overline{\Delta}_q)\Theta Ue^{-i\varphi}-\big[\overline{\Delta}_q(\overline{\Delta}_m+\overline{\Delta}_q)+J^2\big]\Omega_m^2\\&\quad+2(\overline{\Delta}_m+\overline{\Delta}_q)e^{-i\theta}J\Omega_m\Omega_q-e^{-2i\theta}J^2\Omega_q^2\Big|=0.\end{aligned} \tag{13}$$

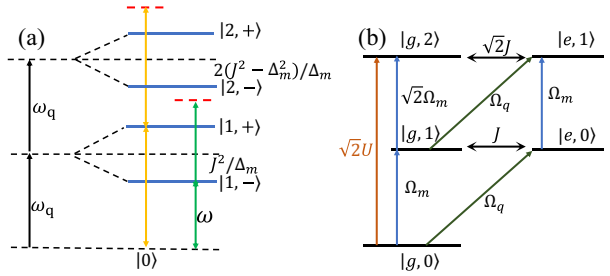


FIG. 2: (a) Energy-level diagram for CMB. (b) Multipath interference scheme for UMB.

The optimal UMB parameters are as follows

$$U = |M|, \qquad \varphi = -\arg(M),$$
$$M = \frac{-2(\overline{\Delta}_m + \overline{\Delta}_q)e^{-i\theta}J\Omega_m\Omega_q + J^2\Omega_q^2 e^{-2i\theta}}{(\overline{\Delta}_m + \overline{\Delta}_q)\Theta} + \frac{(\overline{\Delta}_q(\overline{\Delta}_m + \overline{\Delta}_q) + J^2)\Omega_m^2}{(\overline{\Delta}_m + \overline{\Delta}_q)\Theta}. \tag{14}$$

where $\arg(M) \in (-\pi, \pi]$.

IV. RESULTS

A. Conventional and unconventional magnon blockade in the strong coupling regime

The CMB mechanism relies on the coupling-induced anharmonic level splitting, which destroys the resonance condition for two-magnon excitation [see Fig. 2(a)]. When the qubit driving field satisfies $\omega_q - \omega = J^2/\Delta_m$, this condition enables a transition from the ground state $|g, 0\rangle$ to the lower dressed state $|1, -\rangle$. However, given that $2\omega_q - 2\omega \neq 2(J^2 - \Delta_m^2)/\Delta_m$, the transition from $|1, -\rangle$ to $|2, -\rangle$ is suppressed—a consequence of energy-level repulsion arising from the coupling-induced anharmonicity. To quantify the magnon statistics, we introduce the single-magnon occupation probability P_1 and the mean magnon occupation $\langle n_m\rangle = \langle\hat{m}^\dagger\hat{m}\rangle$. Under the CMB condition, the first-order resonant excitation enhances both P_1 and $\langle n_m\rangle$. This enhancement is a typical signature of CMB.

The UMB effect arises from the destructive interference among distinct excitation pathways. In Fig. 2(b), multiple pathways can lead to the two-magnon state $|g, 2\rangle$: (1) the direct double-excitation path via the magnon parametric drive $|g, 0\rangle \xrightarrow{\sqrt{2}U} |g, 2\rangle$; (2) the cascaded driving path, in which an external field drives the system through the sequential transitions $|g, 0\rangle \xrightarrow{\Omega_m} |g, 1\rangle \xrightarrow{\sqrt{2}\Omega_m} |g, 2\rangle$; (3) mixed paths involving both driving and coupling, including $|g, 0\rangle \xrightarrow{\Omega_m} |g, 1\rangle \xrightarrow{\Omega_q} |e, 1\rangle \xrightarrow{\sqrt{2}J} |g, 2\rangle$, $|g, 0\rangle \xrightarrow{\Omega_q} |e, 0\rangle \xrightarrow{\Omega_m} |e, 1\rangle \xrightarrow{\sqrt{2}J} |g, 2\rangle$, $|g, 0\rangle \xrightarrow{\Omega_q} |e, 0\rangle \xrightarrow{J} |g, 1\rangle \xrightarrow{\Omega_q} |e, 1\rangle \xrightarrow{\sqrt{2}J} |g, 2\rangle$. The probability amplitudes associated with these pathways interfere destructively, causing the two-magnon excitation amplitudes to cancel. As a result, the population of the $|g, 2\rangle$ state is suppressed, thereby realizing UMB.

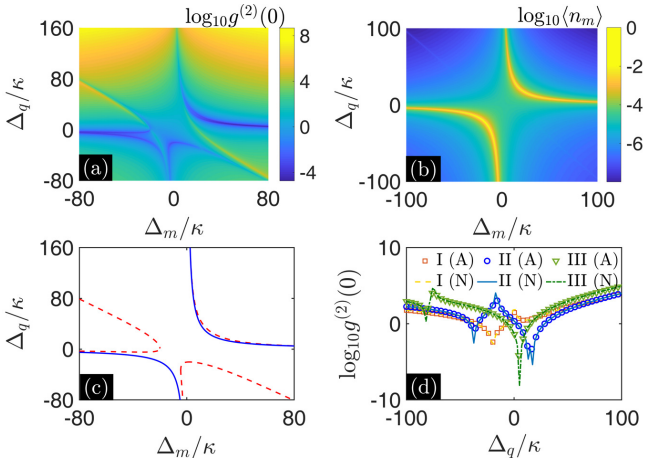


FIG. 3: (a) Equal-time second-order correlation function $g^{(2)}(0)$ and (b) Mean magnon occupation $\langle n_m\rangle$, where $\langle n_m\rangle = \langle\hat{m}^\dagger\hat{m}\rangle$, plotted on a logarithmic scale as functions of Δ_m/κ and Δ_q/κ. Both results are solved by Eqs. (2) and (3). (c) The analytical parameter curves for the CMB in Eq. (7) and the UMB in Eq. (13) are represented by a blue solid line and a red dashed line, respectively. (d) $\log_{10} g^{(2)}(0)$ versus Δ_q/κ for $\Delta_m = -20\kappa$ (I), 30κ (II), and 80κ (III). The blue solid, yellow dashed, and green dashed lines denote the numerical (N) results, while the circles, squares, and triangles correspond to the analytical (A) results. Other parameters are taken as $U = 0.0006\kappa$, $\Omega_m = 0.01\kappa$, $\Omega_q = 0.1\kappa$, $J = 20\kappa$, and $\theta = \varphi = 0$.

To achieve strong magnon antibunching and a high single-magnon occupation probability in the strong-coupling regime, we substitute Eq. (7) into Eq. (14), which yields the CMB-constrained optimal UMB conditions

$$\Delta_q = \frac{J^2}{\Delta_m},$$
$$U = \sqrt{\frac{A\Omega_m^4 + B\Omega_m^3\Omega_q + C\Omega_m^2\Omega_q^2 + D\Omega_m\Omega_q^3 + E\Omega_q^4}{FH}},$$
$$\varphi = \arctan[c, d] - \arctan[a, b], \tag{15}$$

where $A = 2(8J^4 - 3J^2\kappa^2 + 2\kappa^4 + 2(8J^2 + 5\kappa^2)\Delta_q^2 + 8\Delta_q^4 + 2\Delta_m^2(\kappa^2 + 4\Delta_q^2) + 4\Delta_q\Delta_m(4J^2 + \kappa^2 + 4\Delta_q^2))$, $B = -64J[J^2\Delta_m + (J^2 + \kappa^2 + \Delta_m^2)\Delta_q + 2\Delta_m\Delta_q^2 + \Delta_q^3]$, $C = 16J^2[2J^2 + 3\kappa^2 + 2(\Delta_m + \Delta_q)(2\Delta_m + 3\Delta_q)]$, $D = -64J^3\Delta_m - 64J^3\Delta_q$, $E = 16J^4$, $F = (4J^2 + \kappa^2)^2 - 32J^2\Delta_q\Delta_m + 4\kappa^2\Delta_q^2 + 4\Delta_m^2(\kappa^2 + 4\Delta_q^2)$, $H = \kappa^2 + (\Delta_m + \Delta_q)^2$, $a = J^2\Omega_m^2 - \kappa^2\Omega_m^2/2 + \Delta_m\Delta_q\Omega_m^2 + \Delta_q^2\Omega_m^2 - 2J\Delta_m\Omega_m\Omega_q - 2J\Delta_q\Omega_m\Omega_q + J^2\Omega_q^2$, $b = -\kappa\Delta_m\Omega_m^2/2 - 3\kappa\Delta_q\Omega_m^2/2 + 2J\kappa\Omega_m\Omega_q$, $c = -J^2\Delta_m - 3\kappa^2\Delta_m/4 - J^2\Delta_q - 3\kappa^2\Delta_q/4 + \Delta_m^2\Delta_q + \Delta_m\Delta_q^2$, and $d = J^2\kappa + \kappa^3/4 - \kappa\Delta_m^2/2 - 2\kappa\Delta_m\Delta_q - \kappa\Delta_q^2/2$.

In Fig. 3(a), we present the variation of the second-order correlation function $g^{(2)}(0)$ with Δ_m/κ and Δ_q/κ under strong coupling conditions. The blue solid line and the red dashed line in Fig. 3(c) correspond to the optimal condition

curves for CMB and UMB given by Eqs. (7) and (13), respectively. The analytical and numerical results are consistent with each other in Fig. 3(a) over the stated parameter range, with small deviations expected from the two-magnon truncation. These results demonstrate that the UMB mechanism can also achieve MB under the strong-coupling conditions considered here. The resonance behavior of the mean magnon occupation $\langle n_m \rangle$ shown in Fig. 3(b) reflects a typical signature of energy level shifts under strong coupling, supporting the presence of CMB in the system. Figure 3(d) shows the variation of the second-order correlation function $g^{(2)}(0)$ with the qubit detuning Δ_q/κ, where the blue solid, yellow dashed, and green dashed lines denote the numerical (N) results, while the circles, squares, and triangles correspond to the analytical (A) results. The numerical and analytical results are consistent with each other over the plotted range. This indicates that under weak driving and strong coupling conditions, the minimum of $g^{(2)}(0)$ is related to Δ_m and Δ_q.

Figures 4(a) and 4(b) show $g^{(2)}(0)$ as functions of U/κ and Δ_m/κ, and of φ/π and Δ_m/κ, respectively. The white dashed lines are the CMB-constrained optimal UMB conditions given by Eq. (15). The minima follow these lines, indicating that the optimal combinations of the parametric drive amplitude and phase suppress two-magnon excitation through destructive interference. Figure 4(c) compares magnon antibunching and occupation probabilities for CMB and CMB-constrained UMB under the CMB condition $\Delta_q\Delta_m = J^2$ given by Eq. (7), with $U = 2.382 \times 10^{-5}\kappa$ and $\varphi = 0.939\pi$. P_0 is nearly zero, and $P_{n\geq 2}$ is small. At $\Delta_m = 16.7\kappa$, $g^{(2)}(0)$ reaches 2.79×10^{-7}, corresponding to the CMB-constrained optimal UMB condition given by Eq. (15). For $\Delta_m \neq 16.7\kappa$,

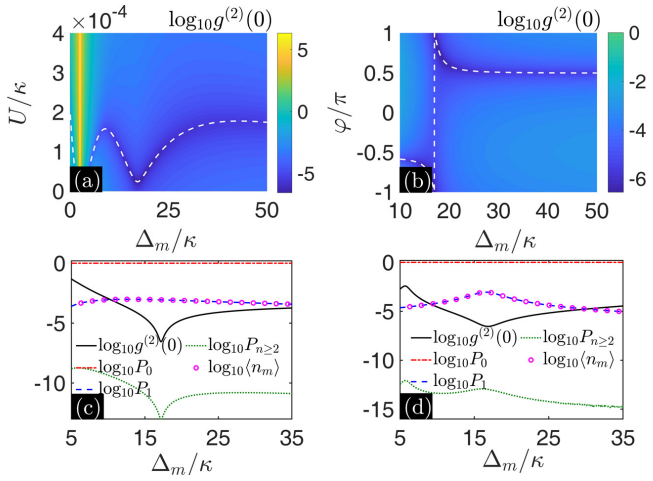


FIG. 4: (a) Logarithmic plots of the equal-time second-order correlation function $g^{(2)}(0)$ versus U/κ and Δ_m/κ. (b) $\log_{10} g^{(2)}(0)$ versus φ/π and Δ_m/κ. (c) $\log_{10} g^{(2)}(0)$, $\log_{10} P_0$, $\log_{10} P_1$, $\log_{10} P_{n\geq 2}$, and $\log_{10}\langle n_m\rangle$ as functions of Δ_m/κ for $U = 2.382 \times 10^{-5}\kappa$ and $\varphi = 0.939\pi$. (d) Same as (c), but for $\Delta_q = 6\kappa$, with U and φ given by Eq. (14). In (a) and (b), U and φ are given by Eq. (15). In (a), the dashed lines indicate the CMB-constrained optimal conditions for UMB. Other parameters are $\Omega_m = 0.01\kappa$, $\Omega_q = 0.04\kappa$, $\theta = 0$, and $J = 10\kappa$.

only the CMB condition is satisfied, while P_1 and $\langle n_m \rangle$ remain high. Figure 4(d) compares UMB and CMB-constrained UMB at $\Delta_q = 6\kappa$. Again, P_0 is nearly zero and $P_{n\geq 2}$ is small. At $\Delta_m = 16.7\kappa$, $g^{(2)}(0)$ reaches 2.79×10^{-7}, and both P_1 and $\langle n_m \rangle$ reach 8.97×10^{-4}, corresponding to the CMB-constrained optimal UMB condition of Eq. (15). For $\Delta_m \neq 16.7\kappa$, only the UMB condition of Eq. (14) is satisfied, and P_1 and $\langle n_m \rangle$ decrease. Figures 4(c) and 4(d) show that the CMB-constrained optimal UMB condition enables coordinated parameter tuning to achieve strong magnon antibunching while enhancing the single-magnon occupation probability.

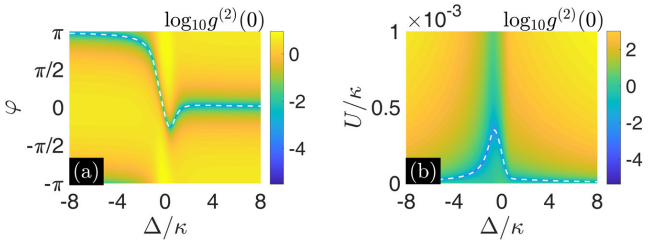


FIG. 5: Logarithmic plots of the second-order correlation function $g^{(2)}(0)$ (solved by Eqs. (2) and (3)) versus Δ/κ and φ with $U^{\rm opt} = |R|$ in (a), and versus Δ/κ and U/κ with $\varphi^{\rm opt} = -\arg(R)$ in (b). The white dashed lines in both panels indicate the optimal UMB condition given by Eq. (16). The other parameters are $\Omega_m = 0.01\kappa$, $\Omega_q = 0.01\kappa$, and $J = 1/\sqrt{2}\kappa$.

B. Unconventional magnon blockade in the weak coupling regime

We now briefly discuss the UMB effect in the weak-coupling regime. For simplicity, we take $\Delta_m = \Delta_q = \Delta$ and set $\theta = 0$. The optimal condition for this case can be obtained by setting Eq. (12) to zero, which gives

$$U^{\rm opt} = |R|, \qquad \varphi^{\rm opt} = -\arg(R),$$
$$R = \frac{4J\overline{\Delta}\Omega_m\Omega_q - J^2\Omega_m^2 - 2\overline{\Delta}^2\Omega_m^2 - J^2\Omega_q^2}{2\overline{\Delta}(J^2 - \overline{\Delta}^2)}, \qquad (16)$$

where $\overline{\Delta} = \Delta - i\kappa/2$ and $\arg(R) \in (-\pi, \pi]$. In the weak-coupling regime, we plot the second-order correlation function $g^{(2)}(0)$ as a function of the parameters Δ/κ, U/κ, and φ, and compare the numerical results with the analytical results from Eq. (16) (white dashed lines), as shown in Fig. 5. Figures 5(a) and 5(b) display $g^{(2)}(0)$ versus φ and Δ/κ, and versus U/κ and Δ/κ, respectively. Figure 5(a) shows pronounced minima (blue regions) near $\varphi = 0$ and $\varphi = \pi$, with $g^{(2)}(0) \ll 1$, corresponding to strong magnon antibunching. Moreover, the minimum region spans a wide range of Δ/κ, indicating that the MB is robust against detuning variations. Figure 5(b) shows that when the parametric drive $U^{\rm opt}$ satisfies the optimal condition with the detuning Δ, MB occurs for any given Δ. The required U for strong antibunching is largest near resonance and decreases away from resonance. Therefore, in the parametrically driven magnon-qubit system, a specific relation between the magnon detuning Δ and the

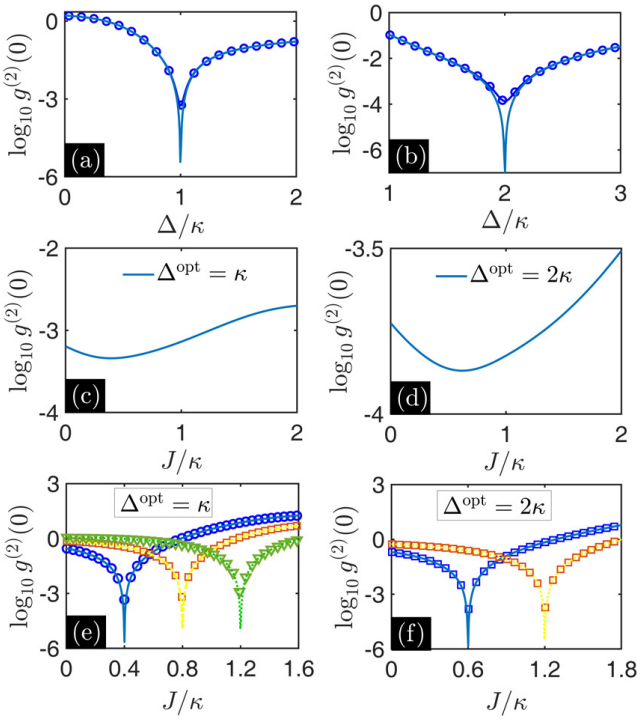


FIG. 6: Logarithm plots of the second-order correlation function $g^{(2)}(0)$ versus Δ/κ under the optimal UPB conditions for (a) $\Delta^{\rm opt}=\kappa$ and (b) $\Delta^{\rm opt}=2\kappa$. $\log_{10} g^{(2)}(0)$ versus J/κ for (c) $\Delta^{\rm opt}=\kappa$ and (d) $\Delta^{\rm opt}=2\kappa$. $\log_{10} g^{(2)}(0)$ versus J/κ with the optimal U and φ from Eq. (15) for $J=0.4\kappa, 0.8\kappa, 1.2\kappa$ in (e) and $J=0.6\kappa, 1.2\kappa$ in (f), under the optimal UPB conditions for $\Delta^{\rm opt}=\kappa$ and $\Delta^{\rm opt}=2\kappa$, respectively. In (a), (b), (e), and (f), the analytical results from Eq. (16) are shown by solid blue, dashed yellow, and dashed green lines, and the numerical results from Eqs. (2) and (3) are shown by circles, squares, and triangles. The parameters are (a) $U_\kappa^{\rm opt}=2.913\times10^{-5}\kappa$, $\varphi_\kappa^{\rm opt}=0.093\pi$, $J=1/\sqrt{2}\kappa$; (b) $U_{2\kappa}^{\rm opt}=2.442\times10^{-5}\kappa$, $\varphi_{2\kappa}^{\rm opt}=-0.018\pi$, $J=1/\sqrt{2}\kappa$; (c) $U^{\rm opt}$ and $\varphi^{\rm opt}$ same as in (a); (d) $U^{\rm opt}$ and $\varphi^{\rm opt}$ same as in (b); (e) $U_1=4.699\times10^{-5}\kappa$, $\varphi_1=-0.035\pi$ for $J=0.4\kappa$; $U_2=2.578\times10^{-5}\kappa$, $\varphi_2=0.145\pi$ for $J=0.8\kappa$; $U_3=2.134\times10^{-5}\kappa$, $\varphi_3=0.402\pi$ for $J=1.2\kappa$; (f) $U_4=2.723\times10^{-5}\kappa$, $\varphi_4=-0.029\pi$ for $J=0.6\kappa$; $U_5=1.413\times10^{-5}\kappa$, $\varphi_5=0.051\pi$ for $J=1.2\kappa$. Other parameters are $\Omega_m=0.01\kappa$ and $\Omega_q=0.01\kappa$.

two-magnon parametric drive strength U, i.e., parametric coordination, is required to achieve destructive interference between the two-magnon excitation pathways and magnon antibunching.

In Figs. 6(a) and 6(b), the equal-time second-order correlation function $g^{(2)}(0)$ is plotted as a function of Δ/κ under the optimal UPB conditions, with the optimal parameters $U^{\rm opt}$ and $\varphi^{\rm opt}$ determined by Eq. (16). Here, $\Delta^{\rm opt}=\kappa$ and $\Delta^{\rm opt}=2\kappa$ are selected as two working points, which correspond to Figs. 6(a) and 6(b), respectively. The analytical predictions yield deeper minima than the numerical simulations, a discrepancy that originates from the two-magnon-state truncation of the Hilbert space. For these two working points, the optimized parameters are $U_\kappa^{\rm opt}=2.913\times10^{-5}\kappa$, $\varphi_\kappa^{\rm opt}=0.093\pi$ for $\Delta^{\rm opt}=\kappa$, and $U_{2\kappa}^{\rm opt}=2.442\times10^{-5}\kappa$, $\varphi_{2\kappa}^{\rm opt}=-0.018\pi$ for $\Delta^{\rm opt}=2\kappa$. Under these optimal conditions, strong magnon antibunching can be achieved in both cases. To examine the effect of the coupling strength J on MB, we present Figs. 6(c) and 6(d), which show the dependence of $g^{(2)}(0)$ on J/κ for detunings $\Delta^{\rm opt}=\kappa$ and $\Delta^{\rm opt}=2\kappa$, respectively. In both cases, as J increases, $g^{(2)}(0)$ exhibits a nonmonotonic trend, first decreasing and then increasing, and reaches a minimum at a specific value. Thus, the optimal MB relies on the cooperative interplay between J and the other system parameters. Figures 6(e) and 6(f) compare the minimal values of $g^{(2)}(0)$ at distinct coupling strengths J/κ for $\Delta^{\rm opt}=\kappa$ and $\Delta^{\rm opt}=2\kappa$, respectively. For $\Delta^{\rm opt}=\kappa$, the minimum at $J=0.4\kappa$ is significantly lower than those at $J=0.8\kappa$ and 1.2κ, with $U_1=4.699\times10^{-5}\kappa$, $\varphi_1=-0.035\pi$ for $J=0.4\kappa$, $U_2=2.578\times10^{-5}\kappa$, $\varphi_2=0.145\pi$ for $J=0.8\kappa$, and $U_3=2.134\times10^{-5}\kappa$, $\varphi_3=0.402\pi$ for $J=1.2\kappa$. For $\Delta^{\rm opt}=2\kappa$, the minimum at $J=0.6\kappa$ is lower than that at $J=1.2\kappa$, with $U_4=2.723\times10^{-5}\kappa$, $\varphi_4=-0.029\pi$ for $J=0.6\kappa$ and $U_5=1.413\times10^{-5}\kappa$, $\varphi_5=0.051\pi$ for $J=1.2\kappa$.

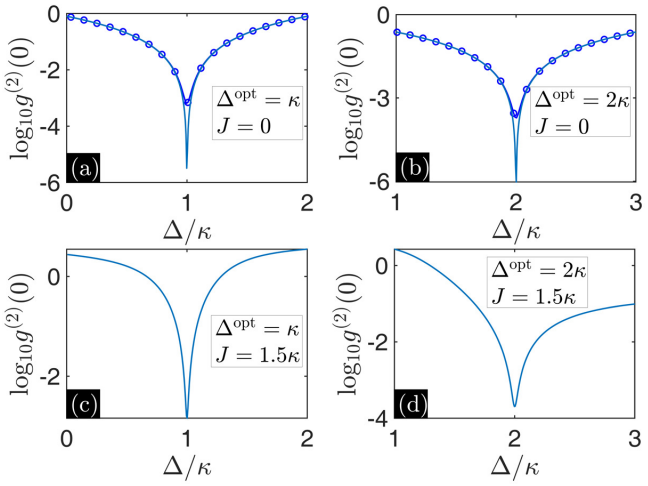


FIG. 7: Logarithm plots of the second-order correlation function $g^{(2)}(0)$ versus Δ/κ under the optimal UPB conditions for (a) $\Delta^{\rm opt}=\kappa$, $J=0$; (b) $\Delta^{\rm opt}=2\kappa$, $J=0$; (c) $\Delta^{\rm opt}=\kappa$, $J=1.5\kappa$; and (d) $\Delta^{\rm opt}=2\kappa$, $J=1.5\kappa$. In (a) and (b), the analytical results from Eq. (16) are shown by solid blue lines, and the numerical results from Eqs. (2) and (3) are shown by circles. The parameters are (a) $U_\kappa^{\rm opt}=8.944\times10^{-5}\kappa$, $\varphi_\kappa^{\rm opt}=-0.147\pi$; (b) $U_{2\kappa}^{\rm opt}=4.851\times10^{-5}\kappa$, $\varphi_{2\kappa}^{\rm opt}=-0.077\pi$; (c) $U_\kappa^{\rm opt}=2.481\times10^{-5}\kappa$, $\varphi_\kappa^{\rm opt}=0.539\pi$; (d) $U_{2\kappa}^{\rm opt}=9.701\times10^{-6}\kappa$, $\varphi_{2\kappa}^{\rm opt}=0.127\pi$. Other parameters are $\Omega_m=0.01\kappa$ and $\Omega_q=0.01\kappa$.

To investigate the feasibility of MB in the absence of magnon-qubit coupling, Figs. 7(a) and 7(b) present the variation of $g^{(2)}(0)$ with Δ/κ at $J=0$ for $\Delta^{\rm opt}=\kappa$ and $\Delta^{\rm opt}=2\kappa$, respectively. Even with zero coupling strength, the system still exhibits pronounced antibunching, and the MB does not show a notable degradation. This effect is attributed to the destructive quantum interference between the cascade-driven transition $|0\rangle\rightarrow|1\rangle\rightarrow|2\rangle$ and the parametric drive pathway $|0\rangle\rightarrow|2\rangle$. The numerical simulations in Figs. 7(c) and 7(d) affirm the validity of the analytical condition under weak driv-

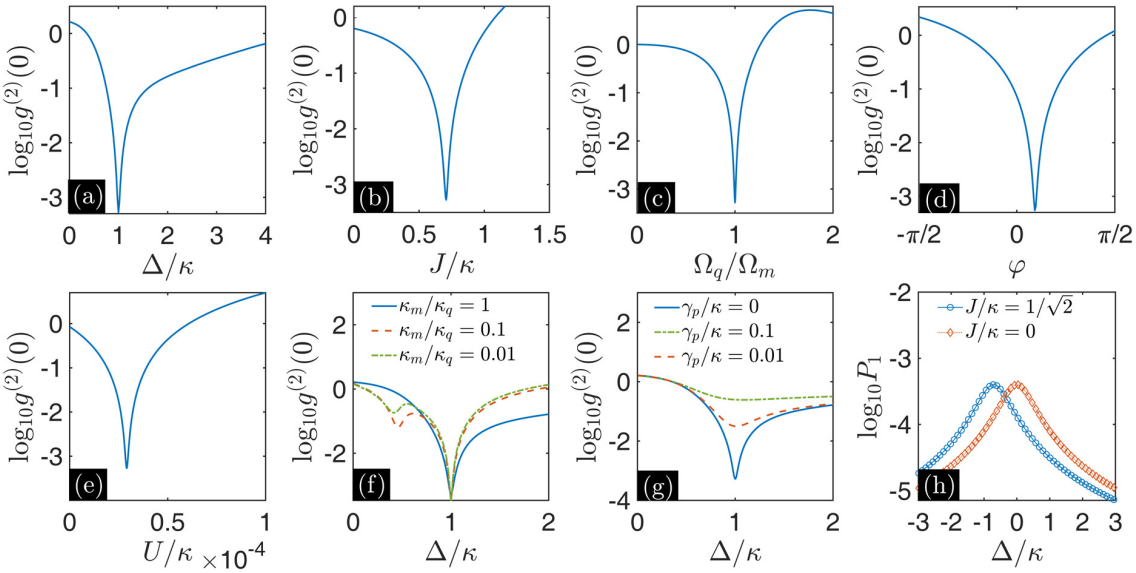


FIG. 8: (a) Logarithmic plot of $g^{(2)}(0)$ versus Δ/κ. (b) $\log_{10} g^{(2)}(0)$ versus J/κ. (c) $\log_{10} g^{(2)}(0)$ versus Ω_q/Ω_m. (d) $\log_{10} g^{(2)}(0)$ versus the relative phase φ. (e) $\log_{10} g^{(2)}(0)$ versus U/κ. (f) $\log_{10} g^{(2)}(0)$ versus Δ/κ for $\kappa_m/\kappa_q = 1$, 0.1, and 0.01. (g) $\log_{10} g^{(2)}(0)$ versus Δ/κ for different pure dephasing rates γ_p/κ. (h) $\log_{10} P_1$ versus Δ/κ for $J = 1/\sqrt{2}\kappa$ and $J = 0$. The parameters are (a) $U^{\rm opt} = 2.913 \times 10^{-5}\kappa$, $\varphi^{\rm opt} = 0.093\pi$, $J = 1/\sqrt{2}\kappa$, $\Omega_m = 0.01\kappa$, and $\Omega_q = 0.01\kappa$; (b) $U^{\rm opt} = 2.913 \times 10^{-5}\kappa$, $\varphi^{\rm opt} = 0.093\pi$, $\Delta = \kappa$, $\Omega_m = 0.01\kappa$, and $\Omega_q = 0.01\kappa$; (c) $U^{\rm opt} = 2.913 \times 10^{-5}\kappa$, $\varphi^{\rm opt} = 0.093\pi$, $J = 1/\sqrt{2}\kappa$, $\Delta = \kappa$, and $\Omega_m = 0.01\kappa$; (d) $U^{\rm opt} = 2.913 \times 10^{-5}\kappa$, $J = 1/\sqrt{2}\kappa$, $\Delta = \kappa$, $\Omega_m = 0.01\kappa$, and $\Omega_q = 0.01\kappa$; (e) $\varphi^{\rm opt} = 0.093\pi$, $J = 1/\sqrt{2}\kappa$, $\Delta = \kappa$, $\Omega_m = 0.01\kappa$, and $\Omega_q = 0.01\kappa$; (f) $J = 1/\sqrt{2}\kappa$, $\Omega_m = 0.01\kappa$, and $\Omega_q = 0.01\kappa$; for $\kappa_m/\kappa_q = 1$, $U_1 = 2.913 \times 10^{-5}\kappa$ and $\varphi_1 = 0.093\pi$; for $\kappa_m/\kappa_q = 0.1$, $U_2 = 5.168 \times 10^{-5}\kappa$ and $\varphi_2 = 0.183\pi$; for $\kappa_m/\kappa_q = 0.01$, $U_3 = 5.436 \times 10^{-5}\kappa$ and $\varphi_3 = 0.201\pi$; (g) $U^{\rm opt} = 2.913 \times 10^{-5}\kappa$, $\varphi^{\rm opt} = 0.093\pi$, $J = 1/\sqrt{2}\kappa$, $\Omega_m = 0.01\kappa$, and $\Omega_q = 0.01\kappa$; (h) $U^{\rm opt} = 2.913 \times 10^{-5}\kappa$, $\varphi^{\rm opt} = 0.093\pi$, $\Omega_m = 0.01\kappa$, and $\Omega_q = 0.01\kappa$.

ing and for coupling strengths satisfying $\kappa < J < 2\kappa$. Fixing the coupling strength at $J = 1.5\kappa$, we plot in Figs. 7(c) and 7(d) $g^{(2)}(0)$ versus Δ/κ under the optimal UPB conditions corresponding to $\Delta^{\rm opt} = \kappa$ and $\Delta^{\rm opt} = 2\kappa$, respectively. The optimal parameters are $U_\kappa^{\rm opt} = 2.481 \times 10^{-5}\kappa$, $\varphi_\kappa^{\rm opt} = 0.539\pi$ for $\Delta^{\rm opt} = \kappa$ and $U_{2\kappa}^{\rm opt} = 9.701 \times 10^{-6}\kappa$, $\varphi_{2\kappa}^{\rm opt} = 0.127\pi$ for $\Delta^{\rm opt} = 2\kappa$. These results indicate that the framework remains valid in the intermediate coupling regime and can induce a pronounced MB.

In Figs. 8(a)–8(c) and 8(g)–8(h), the parametric drive is fixed at $U_\kappa^{\rm opt} = 2.913 \times 10^{-5}\kappa$ and $\varphi_\kappa^{\rm opt} = 0.093\pi$. Figure 8(d) is calculated with U fixed at this value while φ is varied, and Fig. 8(e) with φ fixed at this value while U is varied. Figure 8(a) shows $g^{(2)}(0)$ versus the detuning Δ. As Δ deviates from the optimal value κ, $g^{(2)}(0)$ increases but remains below unity for Δ/κ from 0.35 to 5, where the MB persists, indicating robustness against detuning fluctuations. Figure 8(b) shows $g^{(2)}(0)$ versus J. For J/κ from 0 to 1, $g^{(2)}(0)$ stays below unity and the MB persists, demonstrating a wide tolerance to the coupling strength J, and at zero coupling the parametric drive alone produces antibunching. Figure 8(c) shows $g^{(2)}(0)$ versus the driving-amplitude ratio Ω_q/Ω_m. The MB is strongest at $\Omega_q/\Omega_m = 1$, and blockade occurs for ratios from 0.1 to 1.2. Figure 8(d) shows $g^{(2)}(0)$ versus the relative phase. For relative phases from -0.27π to 0.45π, $g^{(2)}(0)$ remains below unity and the MB persists, indicating a broad tolerance to phase fluctuations. Figure 8(e) shows $g^{(2)}(0)$ versus the parametric drive strength U/κ, where $g^{(2)}(0)$ remains below unity for U/κ from 0 to 6×10^{-5} and the MB persists. At $U/\kappa = 0$, interference among different excitation pathways still suppresses two- and higher-magnon occupations. Figure 8(f) shows $g^{(2)}(0)$ versus the detuning Δ/κ for different dissipation ratios κ_m/κ_q. For $\kappa_m/\kappa_q = 1$, $U_1 = 2.913 \times 10^{-5}\kappa$ and $\varphi_1 = 0.093\pi$; for $\kappa_m/\kappa_q = 0.1$, $U_2 = 5.168 \times 10^{-5}\kappa$ and $\varphi_2 = 0.183\pi$; for $\kappa_m/\kappa_q = 0.01$, $U_3 = 5.436 \times 10^{-5}\kappa$ and $\varphi_3 = 0.201\pi$. All three curves reach their minima at $\Delta/\kappa = 1$, where the MB is strongest. For $\Delta/\kappa > 1$, the case $\kappa_m/\kappa_q = 1$ gives the lowest $g^{(2)}(0)$ and the most pronounced blockade, while $\kappa_m/\kappa_q = 0.1$ and 0.01 give higher $g^{(2)}(0)$ and weaker blockade. The effect of pure dephasing is taken into account by adding a Lindblad term $\mathcal{L}_p(\hat{\rho}) = \gamma_p[2\hat{\sigma}_+\hat{\sigma}_-\hat{\rho}\hat{\sigma}_+\hat{\sigma}_- - (\hat{\sigma}_+\hat{\sigma}_-)^2\hat{\rho} - \hat{\rho}(\hat{\sigma}_+\hat{\sigma}_-)^2]$ to the master equation, where γ_p is the pure dephasing rate of the qubit. Figure 8(g) shows $g^{(2)}(0)$ versus Δ/κ for different γ_p/κ. As γ_p increases, $g^{(2)}(0)$ increases and the MB becomes weaker, but even for $\gamma_p/\kappa = 0.1$, $g^{(2)}(0)$ remains below unity over the displayed detuning range, so antibunching persists. This shows that the MB is robust against pure dephasing. Figure 8(h) shows the single-magnon occupation probability P_1 as a function of the detuning Δ/κ for $J/\kappa = 1/\sqrt{2}$ and $J/\kappa = 0$. The two peaks are at $P_1 \approx 4 \times 10^{-4}$ and are close in height, indicating that the single-magnon occupation probability is nearly the same in the weak-coupling and zero-coupling limits. This shows that the magnon-qubit coupling has little effect on the single-magnon occupation probability.

The proposed scheme is experimentally feasible with cur-

rent superconducting circuit and hybrid magnonics technologies. Direct exchange coupling between a YIG magnon and a superconducting transmon qubit has been realized, with coupling strengths up to $J/2\pi \sim 40$ MHz [9]. Indirect coupling via a microwave cavity gives a magnon-qubit exchange interaction of $J/2\pi \sim$ 10–15 MHz [12, 37] and can cover both the weak- and strong-coupling regimes, e.g., $J/\kappa_m = 0.4$ and $J/\kappa_m = 20$ [95]. The coupling strength J can be tuned by adjusting the size of the YIG sphere, the magnon-qubit distance, and the external magnetic flux. The magnon and qubit frequencies are $\omega_m/2\pi =$ 1–10 GHz and $\omega_q/2\pi =$ 1–10 GHz, controlled by a static magnetic field and an external flux, respectively [9]. The magnon decay rate due to Gilbert damping is $\kappa_m/2\pi =$ 0.1–3 MHz [9, 96]. The coherent driving strength is set to $\Omega/2\pi =$ 10–500 kHz, satisfying the weak-driving condition [97]. A parametrically induced interaction is employed in magnon-qubit experiments to achieve tunable coupling and parametric control [12]. The detuning can be chosen as $\Delta/2\pi = \pm$(1–60) MHz [9].

V. SUMMARY

We study the CMB and UMB effects in the coupled magnon–qubit system under the joint action of coherent and parametric driving. The optimal condition for CMB is derived from the single-magnon resonance condition, while the optimal condition for UMB is obtained by requiring the probability amplitude of the two-magnon state to vanish. In the strong-coupling regime, substituting the CMB condition into the optimal UMB condition yields a phase-tuned CMB-constrained UMB condition. By tuning the phase φ of the parametric drive, one can simultaneously achieve the high single-magnon occupation probability associated with CMB and the strong antibunching associated with UMB. This synergy between high brightness and high purity is important for advancing quantum computation and quantum communication. In the weak-coupling regime, the MB is governed by UMB via multipath destructive interference. Achieving optimal MB relies on a cooperative interplay among the detuning, parametric drive, and coupling strength. Overall, the phase-tunable coexistence in the strong-coupling regime and the parameter-controlled interference in the weak-coupling regime jointly establish a flexible platform for generating strong magnon antibunching.

Acknowledgments

This work was supported by Science and Technology Development Plan Project of Jilin Province (Grant No. 20250102007JC), National Natural Science Foundation of China (NSFC) under Grant No. 12274064, and the Research Start-up Funds of Shenyang Normal University (Grant No. BS202516).

Data Availability Statement

The data that support the findings of this study are included within the article. The numerical solver, truncation, and parameters are described in the Numerical methods section.

[1] Serga A A, Chumak A V and Hillebrands B 2010 *J. Phys. D: Appl. Phys.* **43** 264002
[2] Zheng S, Wang Z, Wang Y, Sun F, He Q, Yan P and Yuan H Y 2023 *J. Appl. Phys.* **134** 151101
[3] Chumak A V, Vasyuchka V, Serga A and Hillebrands B 2015 *Nat. Phys.* **11** 453
[4] Verdú J, Zoubi H, Koller C, Majer J, Ritsch H and Schmiedmayer J 2009 *Phys. Rev. Lett.* **103** 043603
[5] Amsüss R, Koller C, Nöbauer T, Putz S, Rotter S, Sandner K, Schneider S, Schramböck M, Steinhauser G, Ritsch H, Schmiedmayer J and Majer J 2011 *Phys. Rev. Lett.* **107** 060502
[6] Marcos D, Wubs M, Taylor J M, Aguado R, Lukin M D and Sørensen A S 2010 *Phys. Rev. Lett.* **105** 210501
[7] Ranjan V, de Lange G, Schutjens R, Debelhoir T, Groen J P, Szombati D, Thoen D J, Klapwijk T M, Hanson R and DiCarlo L 2013 *Phys. Rev. Lett.* **110** 067004
[8] Eddins A W, Beedle C C, Hendrickson D N and Friedman J R 2014 *Phys. Rev. Lett.* **112** 120501
[9] Kounalakis M, Bauer G E W, and Blanter Y M 2022 *Phys. Rev. Lett.* **129** 037205
[10] Liu Z X, Xiong H and Wu Y 2019 *Phys. Rev. B* **100** 134421
[11] Xie J K, Ma S L and Li F L 2020 *Phys. Rev. A* **101** 042331
[12] Tabuchi Y, Ishino S, Noguchi A, Ishikawa T, Yamazaki R, Usami K and Nakamura Y 2015 *Science* **349** 405
[13] Lachance-Quirion D, Tabuchi Y, Ishino S, Noguchi A, Ishikawa T, Yamazaki R and Nakamura Y 2017 *Sci. Adv.* **3** e1603150
[14] Wolski S P, Lachance-Quirion D, Tabuchi Y, Kono S, Noguchi A, Usami K and Nakamura Y 2020 *Phys. Rev. Lett.* **125** 117701
[15] Lachance-Quirion D, Wolski S P, Tabuchi Y, Kono S, Usami K and Nakamura Y 2020 *Science* **367** 425
[16] Yuan S, Liu C, Chen J, Liu S, Lan J, Yu H, Wu J, Yan F, Yung M H, Xiao J, Jiang L and Yu D 2023 *Phys. Rev. A* **107** 012434
[17] Wang Y P, Zhang G Q, Zhang D, Li T F, Hu C M and You J Q 2018 *Phys. Rev. Lett.* **120** 057202
[18] Zhang G Q, Wang Y P and You J Q 2019 *Sci. China-Phys. Mech. Astron.* **62** 987511
[19] Shen R C, Wang Y P, Li J, Zhu S Y, Agarwal G S and You J Q 2021 *Phys. Rev. Lett.* **127** 183202
[20] Wang Z, Yuan H Y, Cao Y, Li Z X, Duine R A and Yan P 2021 *Phys. Rev. Lett.* **127** 037202
[21] Rao J W, Yao B, Wang C Y, Zhang C, Yu T and Lu W 2023 *Phys. Rev. Lett.* **130** 046705
[22] Wang Z, Yuan H Y, Cao Y and Yan P 2022 *Phys. Rev. Lett.* **129** 107203
[23] Sharma S, Blanter Y M and Bauer G E W 2018 *Phys. Rev. Lett.* **121** 087205
[24] Zhang W, Wang D Y, Bai C H, Wang T, Zhang S and Wang H F 2021 *Opt. Express* **29** 11773
[25] Li J, Zhu S Y and Agarwal G S 2019 *Phys. Rev. A* **99** 021801(R)
[26] Bittencourt V A S V, Feulner V and Kusminskiy S V 2019 *Phys.*

Rev. A **100** 013810
[27] Sun F X, Zheng S S, Xiao Y, Gong Q, He Q and Xia K 2021 *Phys. Rev. Lett.* **127** 087203
[28] Sharma S, Bittencourt V S V and Kusminskiy S V 2022 *J. Phys. Mater.* **5** 034006
[29] He S, Xin X, Zhang F Y and Li C 2023 *Phys. Rev. A* **107** 023709
[30] Yuan H Y, Zheng S, Ficek Z, He Q Y and Yung M H 2020 *Phys. Rev. B* **101** 014419
[31] Mousolou V A, Liu Y, Bergman A, Delin A, Eriksson O, Pereiro M, Thonig D and Sjöqvist E 2021 *Phys. Rev. B* **104** 224302
[32] Fan Y, Li J and Wu Y 2023 *Phys. Rev. A* **108** 053715
[33] Li J, Zhu S Y and Agarwal G S 2018 *Phys. Rev. Lett.* **121** 203601
[34] Amazioug M, Teklu B and Asjad M 2023 *Sci. Rep.* **13** 3833
[35] Yuan H Y, Yan P, Zheng S, He Q Y, Xia K and Yung M H 2020 *Phys. Rev. Lett.* **124** 053602
[36] Qi S F and Jing J 2022 *Phys. Rev. A* **105** 022624
[37] Xu D, Gu X K, Li H K, Weng Y C, Wang Y P, Li J, Wang H, Zhu S Y, You J Q 2023 *Phys. Rev. Lett.* **130** 193603
[38] Zhang X F, Zou C L, Zhu N, Marquardt F, Jiang L and Tang H X 2015 *Nat. Commun.* **6** 8914
[39] Hisatomi R, Osada A, Tabuchi Y, Ishikawa T, Noguchi A, Yamazaki R, Usami K and Nakamura Y 2016 *Phys. Rev. B* **93** 174427
[40] Zhu N, Zhang X, Han X, Zou C L, Zhong C, Wang C H, Jiang L and Tang H X 2020 *Optica* **7** 1291
[41] Sekine A, Ohfuchi M and Doi Y 2024 *Phys. Rev. Appl.* **22** 024071
[42] Cai Q, Liao J, Shen B, Guo G and Zhou Q 2021 *Phys. Rev. A* **103** 052419
[43] Zhang G Q, Wang Y and Xiong W 2023 *Phys. Rev. B* **107** 064417
[44] Chang C, Hobbs T J, Jin D, Li Y, Lisovenko M, Novosad V, Saleem Z H, Trickle T and Wang G 2026 *Phys. Rev. D* **113** 015016
[45] Ullah K, Köse E, Yagan R, Onba¸slı M C and Müstecapıoğlu Ö E 2022 *Phys. Rev. Res.* **4** 023221
[46] Zhou Y H, Liu T, Su Q P, Zhang X Y, Wu Q C, Chen D X, Shi Z C, Shen H Z and Yang C P 2025 *Phys. Rev. Lett.* **134** 183601
[47] Xue W S, Shen H Z and Yi X X 2020 *Opt. Lett.* **45** 4424
[48] Zhou Y H, Zhang X Y, Wu Q C, Ye B L, Zhang Z Q, Zou D D, Shen H Z and Yang C P 2020 *Phys. Rev. A* **102** 033713
[49] Sun J Y and Shen H Z 2023 *Phys. Rev. A* **107** 043715
[50] Liu Q H, Wang G C, Luan T Z and Shen H Z 2024 *Adv. Quantum Technol.* **7** 2300422
[51] Zhou Y H, Zhang X Y, Liu T, Wu Q C, Shi Z C, Shen H Z and Yang C P 2022 *Phys. Rev. Appl.* **18** 064009
[52] Wu Q C, Zhang X Y, Wang Y M, Liu T, Zhou Y H, Shen H Z and Yang C P 2022 *Int. J. Theor. Phys.* **61** 21
[53] Su S L, Tian Y Z, Shen H Z, Zang H P, Liang E J and Zhang S 2017 *Phys. Rev. A* **96** 042335
[54] Shen H Z, Zhou Y H and Yi X X 2015 *Phys. Rev. A* **91** 063808
[55] Zhou Y H, Shen H Z, Zhang X Y and Yi X X 2018 *Phys. Rev. A* **97** 043819
[56] Yang H, Zhou X L, Wang Y X and Yao Z H 2025 *Phys. Rev. Res.* **7** 043003
[57] Qiao X F, Yao Z H and Yang H 2024 *Phys. Rev. A* **110** 053702
[58] Shen H Z, Yang J F and Yi X X 2024 *Phys. Rev. A* **109** 043714
[59] Wang J, Wang Q and Shen H Z 2021 *Europhys. Lett.* **134** 64003
[60] Shen H Z, Wang Q, Wang J and Yi X X 2020 *Phys. Rev. A* **101** 013826
[61] Shen H Z, Shang C, Zhou Y H and Yi X X 2018 *Phys. Rev. A* **98** 023856
[62] Shen H Z, Xu S, Zhou Y H, Wang G C and Yi X X 2018 *J. Phys. B* **51** 035503
[63] Zhou Y H, Shen H Z and Yi X X 2015 *Phys. Rev. A* **92** 023838
[64] Zhou Y H, Wu Q C, Ye B L, Xue L Y and Shen H Z 2019 *Int. J. Theor. Phys.* **58** 472
[65] Wang G C, Shen H Z, Sun C F, Wu C F, Chen J L and Xue K 2017 *J. Mod. Opt.* **64** 583
[66] Zhou Y H and Shen H Z 2017 *Int. J. Theor. Phys.* **56** 2935
[67] Shen H Z, Zhou Y H, Liu D H, Wang G C and Yi X X 2015 *Opt. Express* **23** 32835
[68] Shen H Z, Zhou Y H and Yi X X 2014 *Phys. Rev. A* **90** 023849
[69] Sun H Y, Shang C, Luo X X, Zhou Y H and Shen H Z 2019 *Int. J. Theor. Phys.* **58** 3640
[70] Zhang W, Liu S T, Cui W X, Zhang S and Wang H F 2025 *Phys. Rev. A* **112** 053704
[71] Wang D Y, Bai C H, Liu S T, Zhang S and Wang H F 2019 *Phys. Rev. A* **99** 043818
[72] Wang D Y, Bai C H, Xing Y, Liu S T, Zhang S and Wang H F 2020 *Phys. Rev. A* **102** 043705
[73] Zhang W, Hou R, Wang T, Liu S T, Zhang S and Wang H F 2024 *Phys. Rev. A* **110** 023723
[74] Zhao C, Li X, Chao S, Peng R, Li C and Zhou L 2020 *Phys. Rev. A* **101** 063838
[75] Wang F, Gou C, Xu J and Gong C 2022 *Phys. Rev. A* **106** 013705
[76] Hou R, Zhang W, Han X, Wang H F and Zhang S 2024 *Phys. Rev. A* **109** 033721
[77] Wu K, Zhong W X, Cheng G L and Chen A X 2021 *Phys. Rev. A* **103** 052411
[78] Zhang W, Liu S T, Zhang S and Wang H F 2024 *Phys. Rev. A* **109** 043712
[79] XU Y J, Yang T L, Lin L, and Song J 2021 *J. Opt. Soc. Am. B* **38** 876
[80] Wang Y, Xiong W, Xu Z, Zhang G Q, and You J Q 2022 *Sci. China-Phys. Mech. Astron* **65** 260314
[81] Wang X, Huang K W, and Xiong H 2024 *Phys. Rev. A* **110** 033702
[82] Jaynes E and Cummings F 1963 *Proc. IEEE* **51** 89
[83] Brächer T, Pirro P and Hillebrands B 2017 *Phys. Rep.* **699** 1
[84] Liu L, Moriyma T, Ralph D C and Buhrman R A 2011 *Phys. Rev. Lett.* **106** 036601
[85] Fukami M, Marcks J C, Candido D R, Weiss L R, Soloway B, Sullivan S E, Delegan N, Heremans F J, Flatté M E and Awschalom D D 2024 *Proc. Natl. Acad. Sci. U.S.A.* **121** e2313754120
[86] Jin Z Y and Jing J 2024 *Phys. Rev. A* **110** 012459
[87] Jin Z Y and Jing J 2023 *Phys. Rev. A* **108** 053702
[88] Zhao S, Ren Y L, Hei X L, Pan X F and Li P B 2025 *Phys. Rev. A* **112** 013712
[89] Tang J, Geng W and Xu X 2015 *Sci. Rep.* **5** 9252
[90] Li Z, Li X and Zhong X 2021 *Phys. Rev. A* **103** 043724
[91] Carmichael H, *Statistical Methods in Quantum Optics* (Springer, Berlin, 1999).
[92] Eleuch H 2008 *J. Phys. B: At. Mol. Opt. Phys.* **41** 055502
[93] Plenio M B and Knight P L 1998 *Rev. Mod. Phys.* **70** 101
[94] Minganti F, Miranowicz A, Chhajlany R W and Nori F 2019 *Phys. Rev. A* **100** 062131
[95] Li X Y, Wang X, Wu Z, Yang W X, and Chen A X 2021 *Phys. Rev. B* **104** 224434
[96] Tabuchi Y, Ishino S, Ishikawa T, Yamazaki R, Usami K, and Nakamura Y 2014 *Phys. Rev. Lett.* **113** 083603
[97] Oelsner G, Macha P, Astafiev O V, Il'ichev E, Grajcar M, Hübner U, Ivanov B I, Neilinger P, and Meyer H G 2013, *Phys. Rev. Lett.* **110** 053602